Chemical Science

ROYAL SOCIETY OF CHEMISTRY

EDGE ARTICLE

View Article Online
View Journal | View Issue

Cite this: *Chem. Sci.*, 2024, **15**, 20403

All publication charges for this article have been paid for by the Royal Society of Chemistry

Received 18th September 2024
Accepted 20th October 2024

DOI: 10.1039/d4sc06305h

rsc.li/chemical-science

Bimodal accurate H_2O_2 regulation to equalize tumor-associated macrophage repolarization and immunogenic tumor cell death elicitation†

Yan Zhao,[a] Weiheng Kong,[a] Jianqing Zhu [c] and Fengli Qu *[b]

Simultaneous implementation of tumor-associated macrophage (TAM) repolarization and immunogenic tumor cell death (ICD) elicitation enables tumor immunotherapy with high efficacy. However, the inconsistency of stimulation tolerance restricts simultaneous implementation. To address this obstacle, we validate that an H_2O_2-mediated regulatory strategy could achieve coordinated occurrences. To accomplish this, a bimodal responsive modulator is constructed, namely ZnO_2-ATM (ATM: 3-amino-1,2,4-triazole), as an immune adjuvant to coordinate the occurrence of TAM repolarization and ICD elicitation through the endo/exogenous synergistic responsive production of H_2O_2. H_2O_2 produced by ZnO_2-ATM reverses the immune-suppressive TAM from an M2 to an M1 phenotype, but induces tumor cell necrosis and promotes damage-related molecular pattern release, thereby evoking ICD. This H_2O_2-mediation bimodal responsive therapeutic strategy to induce the synergistic occurrence of TAM repolarization and ICD elicitation promotes effective immune effects against tumors, demonstrating that the ZnO_2-ATM nanoadjuvant could be expected to provide new tools and paradigms for antitumor immunotherapy.

Introduction

Immunotherapy can modulate the tumor microenvironment (TME) and eliminate tumors by activating tumor-immune cycles. Two effective strategies are frequently selected to accomplish this. One modulates the tumor-associated macrophage (TAM) phenotype by repolarizing alternatively activated macrophages (M2) to classically activated macrophages (M1) in order to regulate the host immune response.[1–3] The other one induces a transformation from nonimmunogenic to immunogenic tumor cells by triggering tumor cells to undergo immunogenic cell death (ICD), also stimulating the host immune response.[4,5] This apparent synergy between TAM repolarization and ICD elicitation holds the key to achieving tumor suppression through immunotherapy.[6–8]

Both TAM repolarization and ICD elicitation can be triggered by up-regulating the oxidative stress state of the TME, resulting in tumor-immune cycle activation.[9] Reactive oxygen species (ROS), including hydrogen peroxide (H_2O_2), superoxide ($O_2^{\bullet-}$), singlet oxygen ($^1O_2$), and hydroxyl radicals ($^\bullet OH$), are commonly used as oxidative stress immunomodulators in the TME.[10] Thus far, $^\bullet OH$ generated by the Fenton/Fenton-like effect has been successfully implemented on both tumor cells and macrophages.[11,12] However, different classes of cells have correspondingly different tolerance levels to $^\bullet OH$. Generally, when the $^\bullet OH$ level exceeds the oxidative threshold within tumor cells, ICD can be triggered.[13,14] However, $^\bullet OH$ at high dosage can also trigger peripheral TAM toxicity, cause intracellular DNA double-strand breakage, and affect transcriptional replication, eventually dampening the effect of TAM repolarization immunotherapy and severely limiting the development of synergistic immunotherapy.[15,16] Therefore, it is necessary to maximize the induction of ICD to enhance efficient antitumor immunity, yet, at the same time, also minimize the toxicity of adjuvants to avoid damage to neighboring immune cells. This means that both efficacy and toxicity of immune adjuvants should be precisely optimized to achieve simultaneous implementation of TAM repolarization and ICD elicitation to ensure efficient tumor suppression. Since the ROS dose required by TAM and ICD is very different, it is critical to precisely regulate the ROS to enable efficient activation of both TAM and ICD at the same time.

Tumor cells present an oxidative stress phenotype, and when disturbed by oxidative substances, their toxicity threshold is less than that of TAM cells.[17] However, ROS at low dosage can also present less toxicity and can induce phenotypic plasticity in M1 macrophages. In other words, ROS with less toxic

[a]College of Chemistry and Chemical Engineering, Qufu Normal University, Qufu, Shandong 273165, China. E-mail: qufengli@him.cas.cn

[b]Department of Pathology, Cancer Hospital of Zhejiang Province, Hangzhou Institute of Medicine, Chinese Academy of Sciences, Hangzhou, Zhejiang 310022, China

[c]Department of Gynecologic Oncology, University Cancer Hospital of Chinese Science Academy, Hangzhou, Zhejiang 310004, China

† Electronic supplementary information (ESI) available. See DOI: https://doi.org/10.1039/d4sc06305h

Scheme 1 Schematic diagram of ZnO_2-ATM dissociation, causing the release of Zn^{2+}, H_2O_2 and ATM, and the corresponding intracellular mechanism of H_2O_2 generation.

properties, such as H_2O_2, can avoid genetic damage, maintain TAM repolarization, and retain the ability to induce ICD. Precise modulation of ROS to allow efficient activation of both TAM and ICD at the same time is critical. H_2O_2 can be generated in two ways: exogenous H_2O_2 formation and endogenous H_2O_2 generation.[18,19] Herein, we design an endo/exogenous simultaneous H_2O_2-generating nano-assembly, namely, ZnO_2-ATM (ATM: 3-amino-1,2,4-triazole) with the properties of programmed cleavage and a functional response (Scheme 1). In this system, peroxisomal ZnO_2 maintains a stable exogenous H_2O_2 output, while endogenous H_2O_2 is produced by two pathways. Firstly, cleaved ATM inhibits the activity of catalase (CAT), thereby reducing the conversion from H_2O_2 to O_2. Secondly, released Zn^{2+} acts on mitochondria by promoting the production of $O_2^{\bullet-}$ and H_2O_2 through increased electron leakage of complexes I and III within the mitochondrial electron transport chain.[20] For tumor cells that feature low pH and high glutathione (GSH) content,[21] the rapid reaction of ZnO_2-ATM (H^+/GSH/ATP response properties) keeps tumor cells in a high-dose H_2O_2 environment which can induce ICD to enhance the antitumor immune effect, while the slow reaction of ZnO_2-ATM (ATP response property) maintains a low concentration of H_2O_2 to modulate TAM repolarization. This bimodal response system that combines TAM repolarization and ICD elicitation by ZnO_2-ATM exhibits a promising synergistic immunotherapeutic strategy.

Results and discussion

Tolerance of immune and tumor cells to different ROS patterns

Intracellular oxidative stress in tumor cells can promote tumor proliferation, metastasis, and angiogenesis by regulating a variety of signaling pathways.[22,23] However, higher ROS levels have been found to promote antitumorigenic signaling by initiating oxidative stress-induced tumor cell death.[24] It has also been conjectured that less toxic ROS oxygen-containing compounds, like H_2O_2, compared with the highly toxic $^{\bullet}OH$, could reduce TAM immune cell genetic damage and maintain TAM repolarization. In this therapeutic regime, tumor cells will still undergo oxidative damage, but be closer to the threshold of toxicity than normal cells, such as macrophages, leading, in turn, to the inhibition of tumor cell proliferation and onset of apoptosis/necrosis (Fig. 1A).[25] To perform apoptosis/necrosis assays and evaluate TAM M1 repolarization, the same concentrations of exogenous H_2O_2 and $^{\bullet}OH$ were applied to mouse macrophage RAW264.7 cells and mouse breast 4T1 cancer cells, respectively.

For RAW264.7 cells, within a certain concentration range of ROS (initial concentration of H_2O_2 or $^{\bullet}OH$: 0–20 mM), $^{\bullet}OH$ induced a much greater reduction in cellular activity than H_2O_2 (Fig. 1B). This could be attributed to the high toxicity of $^{\bullet}OH$, but at the same time, this chemical caused significant genetic damage, thereby reducing transcription, translation, and normal cell proliferation. Meanwhile, intracellular peroxidases could degrade exogenous H_2O_2, thus reducing the cellular oxidative stress level. Based on our assays with RAW264.7 cells,

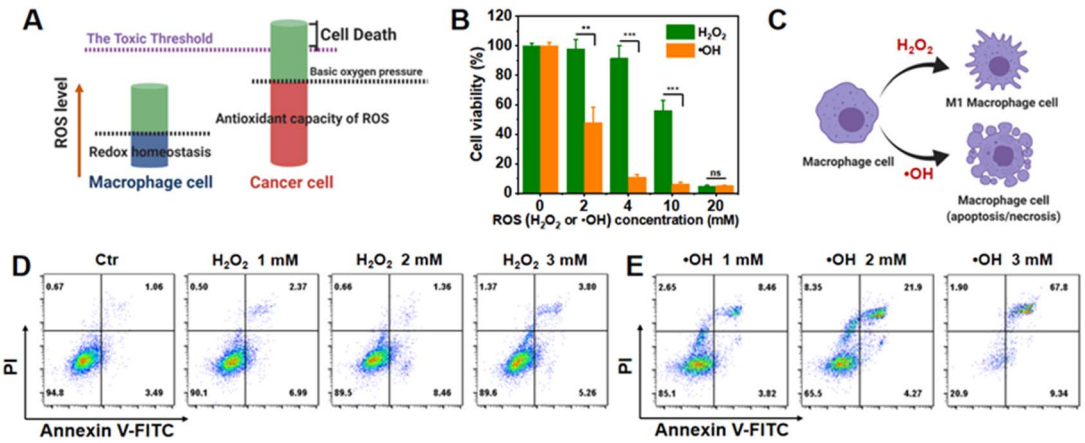

Fig. 1 Differential ROS tolerance in macrophages and tumor cells: effects on viability and apoptosis. (A) Different levels of responsiveness between macrophages and tumor cells to ROS toxicity thresholds. (B) Cell viability of RAW264.7 cells incubated with various concentrations of H_2O_2 or $^{\bullet}OH$. (C) Schematic diagram showing the apoptosis/necrosis of RAW264.7 cells after treatment with different stimuli. The apoptosis/necrosis of RAW264.7 cells after treatment with different concentrations of (D) H_2O_2 or (E) $^{\bullet}OH$ (H_2O_2 or $^{\bullet}OH$ shown was the initially added concentrations).

it was also found that at a limited concentration of H_2O_2 in the range of 1–3 mM, cells underwent apoptosis, albeit in moderation, and importantly, immune M1 repolarization ability was maintained (Fig. 1D and ESI Fig. S1†). Therefore, the lower genetic material damage capacity of H_2O_2, when combined with the greater degree of tolerance to H_2O_2, within the specified concentration range, ensured the continued functioning of RAW264.7 cells (Fig. 1C), as RAW264.7 cells could indeed regulate their own oxidative stress status when faced with low concentrations of H_2O_2, in order to maintain cellular homeostasis and function. Unlike the onset of RAW264.7 cell apoptosis, with increasing concentrations of ROS (H_2O_2 or $^{\bullet}OH$), the degree of necrosis in 4T1 cells gradually increased proportionally (ESI Fig. S2†) based on their lower ROS toxicity threshold.[26] Taken together, this line of evidence, which suggests multiplicity of different ROS patterns in the TME, gives rise to the possibility of designing responsive H_2O_2-generating NPs.

Characterization of the bimodal response to ZnO_2-ATM

To prove aboved hypothesis that different response modes will give different responsive cleaved release, a coordination compound, namely, Zn-ATM, was constructed based on a general metal–organic coordination strategy by self-assembly between Zn^{2+} and ATM mediated by bovine serum albumin (BSA). Transmission electron microscopy (TEM) images revealed the spherical morphology of Zn-ATM with an average diameter of approximately 30 nm (ESI Fig. S3B†). Subsequently, with the addition of H_2O_2 and the adjustment to pH 9.0, peroxide bridge bonds (–O–O–) were formed between the uncoordinated Zn ions within Zn-ATM, generating ZnO_2-ATM with an average diameter of 30 nm (Fig. 2A). Dynamic light scattering (DLS) results revealed that the hydrodynamic diameter of ZnO_2-ATM with a hydrated ionic radius was approximately 100 nm, which showed long-term colloidal stability for more than 14 days (ESI Fig. S4†). For comparison, ZnO_2 without ATM was prepared as the control group using the same procedure. The fluorescence spectrum of ZnO_2-ATM, or Zn-ATM, showed the characteristic fluorescence peak of ATM with a π*–π or π*–n red shift from the electron transfer within the ligand (Fig. 2B).[27] These results confirmed the successful coordination between Zn and ATM and the successful synthesis of ZnO_2-ATM. The stable presence of –O–O– in ZnO_2 and ZnO_2-ATM was further validated by X-ray photoelectron spectroscopy (XPS). O 1s binding energy peaks of ZnO_2 and ZnO_2-ATM both located at 532.6 eV, subordinate to O_2^{2-}, whereas the O 1s binding energy peak of Zn-ATM was located at 530.7 eV, subordinate to O^{2-} (Fig. 2C and ESI Fig. S5†).[28,29]

With its functional –O–O– group, ZnO_2-ATM demonstrated acidic instability potential due to its H_2O_2-derivative-like properties, as shown in ESI Fig. S6.† The spherical and regular ZnO_2-ATM morphology was completely disrupted, generating an irregular lamellar structure after 24 h of incubation at pH 5.0. In addition, the oxidizing environment during synthesis rendered ZnO_2-ATM potentially unstable under reducing conditions. Considering the coordination force between ATP and Zn^{2+}, ZnO_2-ATM had potential ATP-responsive properties. To verify the potential responsive behavior of ZnO_2-ATM, we measured the release of Zn^{2+} and the generation of H_2O_2 from ZnO_2-ATM under acidic conditions (pH 5.0), as well as in an aqueous GSH solution (final concentration, 20 μg mL^{-1}) and an aqueous ATP solution (final concentration, 500 μg mL^{-1}).

As shown in Fig. 2D and ESI Fig. S7,† compared to the stable dispersed NPs at pH 7.4, Zn^{2+} from Zn-ATM, ZnO_2, and ZnO_2-ATM was rapidly released at pH 5.0. The releasing equilibrium was achieved in less than 5 h, indicating that these corresponding NPs were completely cleaved. Compared to ZnO_2, the faster responses of Zn-ATM and ZnO_2-ATM to GSH or ATP were largely a result of the metal (Zn^{2+}) of Zn-ATM and ZnO_2-ATM, which possessed larger contact areas with GSH or ATP for a faster response. In addition, compared to normal cells, such

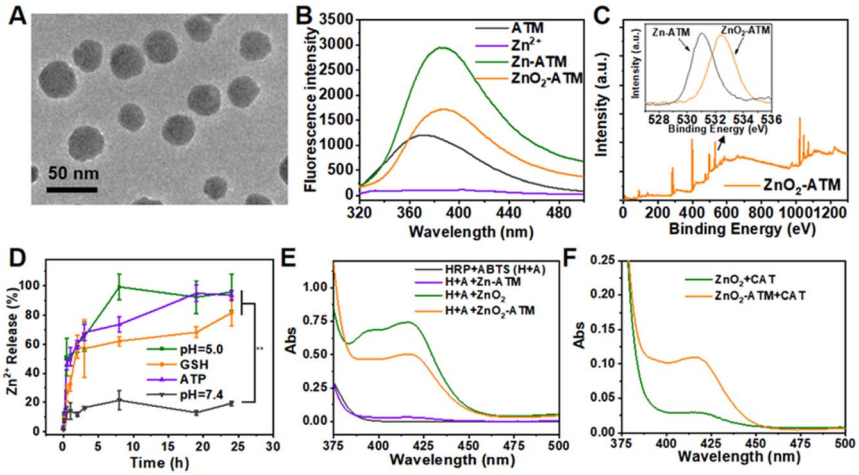

Fig. 2 Characterization of ZnO_2-ATM nanoparticles: morphology, ROS generation, and stability. (A) TEM image of ZnO_2-ATM. (B) FL spectrum of ZnO_2-ATM. (C) XPS survey spectrum of ZnO_2-ATM with the inset showing the O 1s XPS spectra of Zn-ATM and ZnO_2-ATM. (D) Zn^{2+} release from ZnO_2-ATM after incubation under different solution conditions. (E) H_2O_2 generation after incubation with different NPs (chromogenic changes due to ABTS). (F) Effect of ZnO_2 or ZnO_2-ATM on the yield of H_2O_2 in the presence of CAT (chromogenic changes due to ABTS).

as immune cells (pH 7.0, GSH: 10 μM; ATP: 200 μg mL^{-1}), tumor cells possessed an acidic environment (pH 4.5–6.5) and high concentrations of reducing agents (GSH: 2–10 mM). To this end, we investigated the response changes of NPs between the emulated tumor cell environment (H^+/GSH/ATP) and the emulated immune cell environment (ATP) *in vitro*. As shown in ESI Fig. S8,† the response rates of ATP-responsive NPs were significantly lower than those of H^+/GSH/ATP triplet-response NPs, with more than 50% of the ATP-responsive NPs remaining stable after 24 h.

Similarly, H^+ could affect the stability of –O–O– formed in ZnO_2-ATM, causing the breakage of –O–O– and forming H_2O_2.[30,31] The ability of ZnO_2-ATM to generate H_2O_2 was examined by the oxidative changes in the color-emitting substrate 2,2′-azino-bis(3-ethylbenzthiazoline-6-sulfonic acid) (ABTS) after HRP-catalyzed conversion from H_2O_2 to $^{\bullet}OH$. As shown in Fig. 2E, –O–O– in ZnO_2 and ZnO_2-ATM could generate H_2O_2 under acidic conditions. Under the same criteria, the amount of generated H_2O_2 by ZnO_2-ATM was lower than that by ZnO_2, mainly by the unliganded Zn^{2+} from the coordination compound of Zn-ATM, which could form peroxides with –O–O– during ZnO_2-ATM assembly. Furthermore, the kinetic rate of H_2O_2 production by ZnO_2-ATM in the emulated tumor and immune cells was consistent with the aforementioned Zn^{2+} release (ESI Fig. S9†). As a peroxidase (CAT) inhibitor, ATM enhanced intracellular H_2O_2-based ROS oxidative stress by attenuating the ability of CAT to catalyze H_2O_2 and form O_2, as shown in ESI Fig. S10A.† The ability of CAT to catalyze O_2 production was dramatically reduced after 2 h of coincubation within ATM. Similarly, the released ATM from Zn-ATM and ZnO_2-ATM under acidic conditions also inhibited the catalytic ability of CAT to some extent (ESI Fig. S10B†). In addition, after coincubation of ZnO_2 or ZnO_2-ATM with CAT, the H_2O_2 produced by ZnO_2 was completely consumed by CAT, while the H_2O_2 produced by ZnO_2-ATM was still viable owing to the inhibition of ATM (Fig. 2F). These results showed that ZnO_2-ATM, as responsive NPs, could perform bimodal functions in different cellular environments.

In vitro TAM M1 repolarization and ICD elicitation

It was demonstrated that ZnO_2-ATM has triplet-response (H^+/GSH/ATP) potential *in vitro*. Here, ZnO_2-ATM NPs were used to generate exogenous H_2O_2 to elevate oxidative stress at the cellular level. H_2O_2 could promote the activation and regulation of immune responses by inducing ICD and affecting the polarization state of macrophages. In this process, H_2O_2 played a key role by influencing the modes of cell death, regulating the

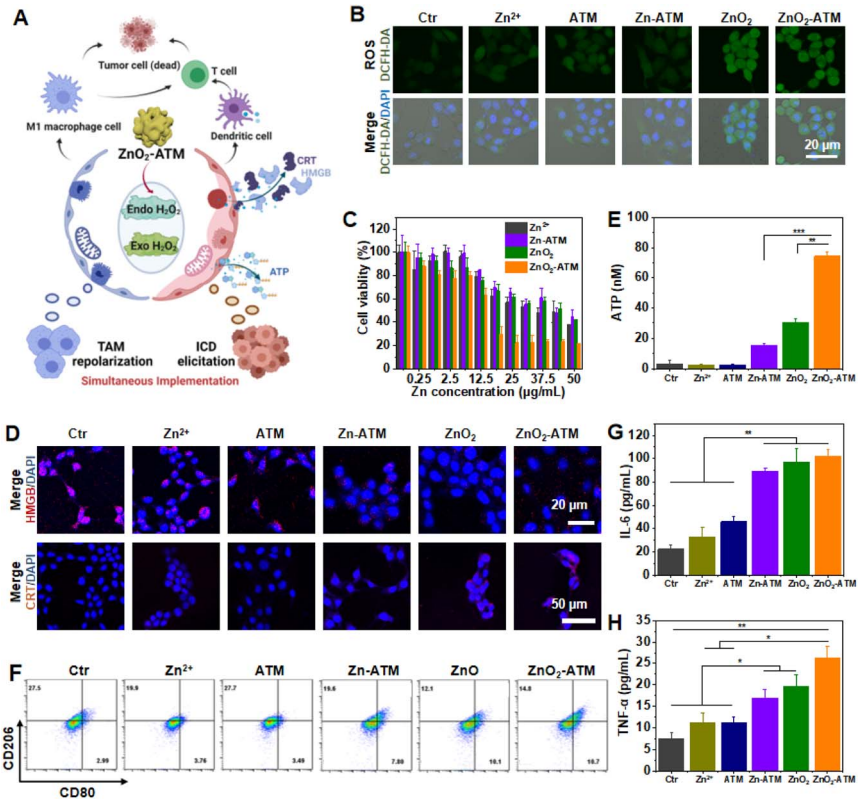

Fig. 3 Bimodal regulation of H_2O_2 by ZnO_2-ATM: coordination of TAM repolarization and ICD elicitation. (A) Schematic of ZnO_2-ATM achieving endo/exogenous H_2O_2 bimodal regulation to coordinate TAM repolarization and ICD elicitation. (B) Confocal images of DCFH-DA-stained 4T1 cells after various treatments (green: ROS; blue: nucleus). (C) Cell viability of 4T1 cells incubated with different concentrations of NPs (quantified by using Zn). (D) Confocal images of HMGB- and CRT-stained 4T1 cells after various treatments. (E) Release of ATP from 4T1 cells after various treatments. (F) Population changes of RAW264.7 M1 ($CD80^{high}CD206^{low}$) macrophages after various treatments. Quantification of cytokine (G) IL-6 and (H) TNF-α secretion of RAW264.7 cells after various treatments.

metabolism and signaling pathways of macrophages, and promoting immune activation.[32] In brief, 2′,7′-dichlorodihydrofluorescein diacetate (DCFH-DA) was used as an intracellular ROS probe. Compared with control group cells, ZnO_2- and ZnO_2-ATM-treated cells showed stronger green fluorescence intensity, demonstrating the sufficient production of H_2O_2. Yet, Zn-ATM NPs without –O–O– showed only negligible fluorescence enhancement compared with other groups, mainly owing to the absence of potential exogenous H_2O_2 production (Fig. 3B). Subsequently, cell viability was quantified by the 3-[4,5-dimethylthiazol-2-yl]-2,5-diphenyl tetrazolium bromide (MTT) assay (Fig. 3C and ESI Fig. S11†). When 4T1 cells were treated with Zn-ATM or ZnO_2 (25 μg mL^{-1} of Zn), their survival rates were reduced by 40%. Comparatively, after treatment with ZnO_2-ATM (25 μg mL^{-1} of Zn), over 75% of 4T1 cells were suppressed, indicating the synergistic effects among Zn^{2+}, H_2O_2, and ATM on the increased oxidative damage to 4T1 cells.

The increased exogenous H_2O_2 generation in tumor cells can increase immunogenicity, eventually leading to tumor cell apoptosis. This process is known as immunogenic cell death (ICD). ICD is characterized by significant changes in mitochondrial ATP, and proteins, such as calreticulin (CRT) and high mobility group box 1 (HMGB), can induce DC cell maturation and antigen presentation to activate cytotoxic T lymphocytes (CTLs) for better therapeutic effects (Fig. 3A). As shown in Fig. 3D, in the steady state (control), HMGB was shuttled between the cytoplasm and the nucleus. Then, after ZnO_2-ATM was introduced, the generated H_2O_2 could disrupt oxidative homeostasis, damage the plasma membrane and nucleus, and promote HMGB exposure on the cell surface by diffusion. The exposed HMGB could bind to DC receptors and activate inflammatory pathways. CRT, a calcium-binding protein critical for signal regulation and internal environmental homeostasis, was activated by H_2O_2 produced by ZnO_2-ATM and exposed on the surface of the cell membrane to recruit and stimulate DC cell maturation with "eat me" signals. Moreover, the exposed CRT could induce the production and release of inflammatory factors and chemokines, which, together with the induction of macrophage activation, could promote the release of proinflammatory factors, such as TNF-α and IL-6. Under stress conditions involving H_2O_2 production by ZnO_2-ATM, large amounts of ATP were released from 4T1 cells into the extracellular environment (Fig. 3E), thereby inducing an immune response with "find me" signals that could rapidly recruit DC cells to the tumor area for the enhancement of the antitumor immune effect.[33,34] The extracellular release of ATP, a hallmark event of early-stage apoptosis, indicated that mitochondrial integrity had been disrupted.[35,36] Here, the mitochondrial integrity of 4T1 cells was examined by JC-1 staining. As shown in ESI Fig. S12,† a change in staining from red to green fluorescence (ZnO_2-ATM *vs.* Ctr) implied a decrease in the mitochondrial membrane potential. For untreated cells, the ratio of green to red fluorescence (G/R) was 0.365, and after incubation with ZnO_2-ATM, the G/R value increased to 2.035. This marked change in the G/R value reflected the mitochondrial dysfunction of ZnO_2-ATM to tumor cells. It is also worth mentioning that the addition of Zn^{2+} elevated the G/R value because Zn^{2+} could act on mitochondria and affect electron transport. In conclusion, responsive ZnO_2-ATM contributed to mitochondrial imbalance and induced ICD in tumor cells at the cellular level through the synergism among Zn^{2+}, ATM, and H_2O_2.

The immunosuppressive properties of the TME severely inhibited the immunotherapeutic effect, converting macrophages from "cold" M2 phenotypes to inflammatory "hot" M1 phenotypes, essentially creating a key challenge for antitumor immunotherapy. However, our experiments have shown that intracellular oxidative stress encouraged phenotypic plasticity and could activate macrophages to enter the M1 phenotype state (Fig. 1A). Here, we hypothesized that ZnO_2-ATM NPs with H_2O_2-generating capacity could induce macrophages to the M1 phenotype. RAW264.7 cells could repolarize to the M1 phenotype after treatment with lipopolysaccharide (LPS, a positive control) (the number of M1, $CD80^{high}CD206^{low}$), and to the M2 phenotype after treatment with interleukin 4 (IL-4, a negative control) (ESI Fig. S13†). To validate our hypothesis, RAW264.7 cells were incubated with Zn^{2+} or Zn-ATM. A rare uptick in M1 repolarization was detected because Zn^{2+} induced restricted oxidative stress in mitochondria. For ZnO_2 and ZnO_2-ATM, which could produce substantial H_2O_2, M1 repolarization increased to 10.1% and 10.7% from 2.99%, respectively, indicating that the TAM M1 repolarization effect was ensured by the synergism between Zn^{2+} and H_2O_2 (Fig. 3F). Above all, the selected adjuvants with H_2O_2 production ability reached a practical usage for simultaneous TAM M1 repolarization and ICD elicitation, helping to coordinate these two occurrences. In addition, M1 repolarized macrophages can release proinflammatory cytokines, such as IL-6 and TNF-α, to enhance the immune response.[37,38] As shown in Fig. 3G and H, incubation of ZnO_2-ATM with RAW264.7 cells increased IL-6 and TNF-α secretion by 4.57-fold and 3.50-fold, respectively. Thus, ZnO_2-ATM with Zn^{2+} and H_2O_2 production capacity could reverse the immunosuppressive TME by upregulating oxidative stress.

In vivo immune system activation and anti-metastasis immunotherapy

Achieving simultaneous implementation of TAM repolarization and ICD stimulation was a key challenge in current tumor immunotherapy. Conventional therapeutic strategies were often limited by inconsistencies in stimulus tolerance. The design advantage of ZnO_2-ATM lies in its ability to stably generate H_2O_2, both to reverse the immunosuppressive TAM and to induce tumor cell necrosis and promote the release of damage-associated molecular patterns that trigger ICD. Compared with previous studies where TAM M1 repolarization and ICD elicitation were not fully compatible, the as-mentioned *in vitro* experiments demonstrated that ZnO_2-ATM with responsive Zn^{2+}, ATM, and H_2O_2 generation ability could simultaneously induce M1 repolarization and ICD elicitation. Here, we proceeded to investigate the antitumor effect of ZnO_2-ATM *in vivo*, as well as immune system activation and antimetastatic efficacy. After intratumoral injection of various NPs, it was evident that ZnO_2-ATM had a significant tumor growth

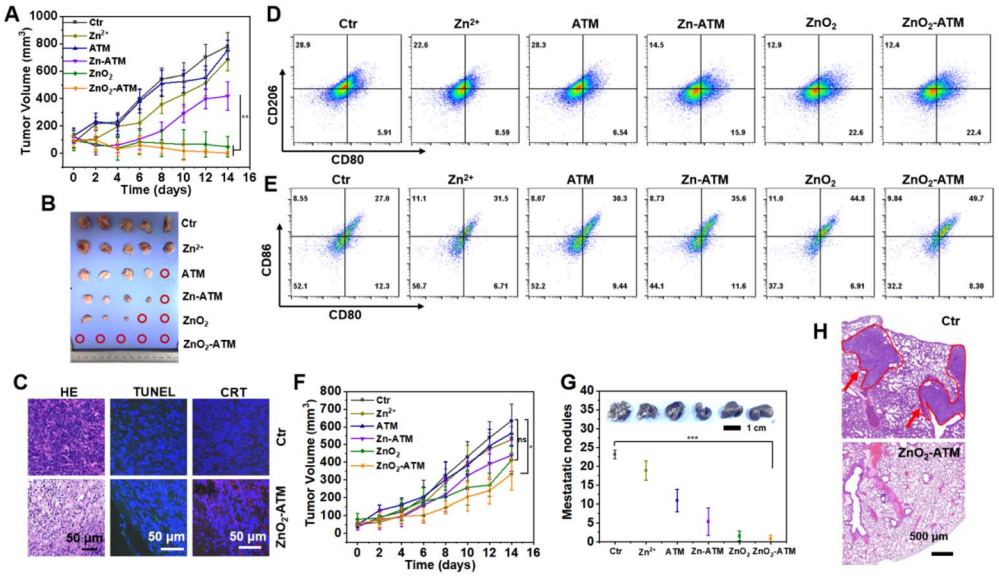

Fig. 4 *In vivo* antitumor efficacy of ZnO_2-ATM: inhibition of metastatic tumor growth and immune activation. (A) Primary tumor growth curves of various treatment groups. (B) Images of excised primary tumors after sacrificing mice at 14 days post-injection. (C) H&E-, TUNEL- and CRT-stained immunofluorescence of primary tumor sections at 1 day post-injection after ZnO_2-ATM treatment. (D) Population changes of M1 ($CD80^{high}CD206^{low}$) macrophages in primary tumors after various treatments at 3 days post-injection. (E) Population changes of maturing DCs ($CD80^{high}CD86^{high}$) in spleens after various treatments at 3 days post-injection (gating on $CD11c^{+}$). (F) Distant tumor growth curves of various treatment groups. (G) Number of metastatic nodules in lungs after various treatments with the inset graph showing the corresponding lungs with metastatic nodules. (H) H&E-stained lung sections at 44 days post-injection. Red arrows indicate metastases.

inhibitory effect on primary tumors (Fig. 4A, B and ESI Fig. S14†) owing to the synergistic effect of Zn^{2+}, ATM, and H_2O_2, which could enhance oxidative stress to stimulate tumor cell apoptosis. Furthermore, the body weight of mice from each group remained unchanged during 14 days of observation (ESI Fig. S15†), indicating that these therapeutic adjuvants did not cause any significant acute damage to liver or kidneys. Meanwhile, hematoxylin and eosin (H&E) histological staining of these representative organs showed no obvious pathological damage (ESI Fig. S16†). The efficient inhibition of primary tumors by ZnO_2-ATM could also be visualized in pathological sections. As shown by H&E histologically stained sections in Fig. 4C and ESI Fig. S17–S19,† obvious cell atrophy and necrosis with crinkled nuclei occurred after 1 day of ZnO_2-ATM treatment. Similarly, terminal deoxynucleotidyl transferase dUTP nick end labeling (TUNEL) showed green fluorescence, indicating that ZnO_2-ATM had caused significant damage to the cytogenetic material, leading to apoptosis/necrosis. In CRT immunofluorescence staining, the enhanced red fluorescence signal implied the occurrence of ICD within tumor cells accompanied by apoptosis/necrosis.

Compared with the control group, treatment with ZnO_2-ATM remarkably upregulated the population of repolarized M1 (Fig. 4D), the occurrence of ICD, and the increase in M1-type TAM, accompanied by the increased secretion of proinflammatory cytokines (IL-6 and TNF-α) by 5.67-fold and 2.67-fold, respectively (ESI Fig. S20†). All these data suggested that ZnO_2-ATM NPs could successfully reverse the immunosuppressive TME by elevating intratumoral oxidative stress.

Released antigens can promote DC cell maturation, thereby increasing T cell infiltration within both primary and metastatic tumors.[39] DC cells, as specialized antigen-presenting cells *in vivo*, can activate T cells by presenting antigens and regulating other immune cell functions by secreting cytokines/chemokines.[40] As shown in Fig. 4E, after the ZnO_2-ATM treatment, the maturation rate of DC cells increased owing to the onset of intratumoral ICD. Subsequently, DC cells secreted a variety of cytokines/chemokines to promote the infiltration of effector T cells within the TME. For primary tumors in the control group, the infiltration of T helper (Th) cells and CTLs was minimal, but ZnO_2-ATM elevated the populations of Th cells (CD4) and CTLs (CD8a) by 2.39-fold and 3.16-fold, respectively (ESI Fig. S21†). These findings indicated that ZnO_2-ATM had successfully altered the microenvironment of immunosuppressive tumors by increasing oxidative stress within the tumors. Effector T cells can act on both primary and metastatic tumors. To determine the role of ZnO_2-ATM in activating antitumor immunity, we assessed the ZnO_2-ATM-induced immune environment of distant tumors. Similar to the T-cell infiltration features of primary tumors, ZnO_2-ATM induced a 3.43-fold and 4.06-fold increase in the populations of Th cells (CD4) and CTL cells (CD8a), respectively, in the metastatic tumor (ESI Fig. S22†), indicating that the activation of antitumor immunity promoted the regression of metastatic tumors. Here, by observing the treatment process, the growth of metastatic tumors was inhibited as the primary tumors gradually shrank until eradication (Fig. 4F). Meanwhile, histological analysis showed that the metastases induced by ZnO_2-ATM were also accompanied by apoptosis/necrosis (ESI Fig. S23†).

A proportion of antigen-activated T cells was characterized by the conversion to memory T cells.[41,42] As shown in ESI Fig. S24,† compared with the control group, ZnO_2-ATM induced a significant increase in the population of memory T cells, from 6.06% to 18.6%. The increased memory T cells supported the potential antitumor metastatic ability of ZnO_2-ATM. To evaluate the anti-metastatic efficacy of ZnO_2-ATM, 4T1 cells were injected intravenously into mice after 18 days of intratumoral treatment (ESI Fig. S25†) to establish a metastatic tumor model. The survival results confirmed that ZnO_2-ATM-based immunotherapy could significantly reduce the risk of tumor recurrence/metastasis and prolong the lifespan of mice with a survival rate of over 80%, which was significantly higher than that of the control group (ESI Fig. S26†). After 44 days of treatment, the lungs from each group were stained, and tumor metastasis was assessed by counting tumor nodules in the lungs. ZnO_2-ATM could inhibit tumor metastasis compared with the other groups (Fig. 4G, H and ESI Fig. S27†). These findings confirmed that ZnO_2-ATM-based oxidative immunotherapy could successfully induce an immune memory effect to inhibit tumor metastasis.

Current immunotherapy strategies have been remarkably effective in modulating the TME to activate the tumor-immunity. However, the differential ROS tolerance of TAM repolarization and ICD excitation limited the effectiveness of their synergistic implementation. ZnO_2-ATM was introduced to address these challenges. Its bimodal generation of H_2O_2 enabled effective activation of TAM and ICD without damaging immune cells. Compared to conventional strategies, ZnO_2-ATM mediated immunomodulation with less toxic ROS, avoided genetic damage, and maintained the repolarizing capacity of TAM while retaining the ability to induce ICD. This precise ROS modulation allowed ZnO_2-ATM to improve anti-tumor immune efficiency while reducing the toxicity of the immune adjuvant, demonstrating its great potential in overcoming the limitations of current immunotherapies.

Experimental

Materials

H_2O_2, 3-amino-1,2,4-triazole (ATM), a JC-1 staining kit, and dimethyl sulfoxide (DMSO) were purchased from Sinopharm Chemical Reagent Co., Ltd. Catalase (200 U mg^{-1}) (CAT), horseradish peroxidase (HRP), bovine serum albumin (BSA), adenosine triphosphate (ATP), reduced glutathione (GSH), and 2,2′-azino-bis(3-ethylbenzothiazoline-6-sulfonic acid) (ABTS) were purchased from Aladdin Reagents Company (Shanghai, China). Hoechst and DAPI were obtained from Sigma-Aldrich Co. (St. Louis, MO, USA). An ATP assay kit was obtained from Nanjing Jiancheng Biotech Co., Ltd. Lipopolysaccharide (LPS) and mouse interleukin 4 (IL-4) recombinant protein were obtained from ThermoFisher Scientific (Waltham, USA). CRT antibodies, HMGB-1 antibodies, APC-conjugated CRT secondary antibodies and Alexa Fluor 594-conjugated HMGB secondary antibodies were purchased from Univ Biotech Co., Ltd. 3-(4,5-Dimethylthiazol-2-yl)-2,5-diphenyltetrazolium bromide (MTT) was obtained from Biofrox Co., Ltd. A TUNEL apoptosis detection kit (C1086) was purchased from Beyotime Biotechnology Co., Ltd. A TNF-α ELISA kit, an IL-6 ELISA kit, APC-conjugated anti-mouse CD80 (CD80-APC), FITC-conjugated anti-mouse CD11b (CD11b-FITC), FITC-conjugated anti-mouse CD11c (CD11c-FITC), PE-conjugated anti-mouse CD206 (CD206-PE), APC-conjugated anti-mouse CD3 (cat. 100236), PE-conjugated anti-mouse CD4 (CD4-PE), FITC-conjugated anti-mouse CD8a (CD8a-FITC), PE-conjugated anti-mouse CD86 (CD86-PE), and PE-conjugated anti-mouse CD44 (CD44-PE) were obtained from Multi-Science Co., Ltd. Annexin V-FITC/propidium iodide (PI) and 2,7-dichlorodihydrofluorescein diacetate (DCFH-DA) were purchased from Yeasen Co., Ltd. Deionized water was generated using a Millipore Milli-Q system (Billerica, MA, USA). Deionized water was used throughout the experiments. All chemicals were used without further purification.

Characterization

Transmission electron microscope (TEM) images were obtained from a TEM system (JEOL, JEM-2100Plus) with an accelerating voltage of 200 kV. The mean diameter and zeta potential of the as-prepared nanoparticles were measured by dynamic laser light scattering (ZEN 3600, Malvern Instruments). Dissolved oxygen in solution was measured by using a Hanna microcomputer dissolved oxygen (DO) meter (HI9146). Concentrations of zinc were measured by using inductively coupled plasma–mass spectroscopy (ICP-MS, Agilent, 8900). Cells were imaged through a confocal laser scanning fluorescence microscope (Nikon, Ti-E + A1R MP). MTT assay was performed using a Spectramax microplate reader (Molecular Devices, iD5). Fluorescence spectra were obtained on a Hitachi Fluorescence Spectrometer (F-4600). X-ray photoelectron spectroscopy (XPS) analysis was performed using a Thermo ESCALAB 250XI. The UV/vis spectrum was recorded on a Shimadzu UV-3600 spectrophotometer. Cell collection analysis was performed on a flow cytometer (BD C6 Plus). The cell pictures of diagrams were created with **https://www.biorender.com/**.

Synthesis of ZnO_2-ATM NPs

0.5 mg of BSA and 16.8 mg of ATM (0.2 mmol) were dissolved in 5 mL of water. Then, 5 mL of water containing 12 mg of $Zn(NO_3)_2 \cdot 6H_2O$ (0.04 mmol) were added dropwise with vigorous stirring for 0.5 h. The resulting Zn-ATM NPs were washed several times and then redispersed in water.

The pre-prepared aqueous solution of Zn-ATM NPs was redispersed in 2 mL of water and mixed with 0.2 mL of H_2O_2. The pH of the reaction solution was adjusted to 9.0 by using NaOH. After stirring at room temperature for another 4 h, the obtained ZnO_2-ATM NPs were washed several times with ethanol and collected by centrifugation. The Zn content in ZnO_2-ATM was quantified by ICP-MS.

Decomposition of ZnO_2-ATM NPs

The release of Zn^{2+} from ZnO_2-ATM NPs was determined by dialysis (3.5 KD). The aqueous solution of ZnO_2-ATM NPs was dialyzed against MES buffer (pH = 5.0), 500 μg mL^{-1} of ATP solution, and 20 μg mL^{-1} of GSH or PBS buffer (pH = 7.4),

respectively. The released Zn^{2+} was measured by ICP-MS. The release of Zn^{2+} from Zn-ATM or ZnO_2 was measured using the same procedure.

The generation of H_2O_2 from ZnO_2-ATM NPs was determined by a mediated colorimetric ABTS strategy at pH = 5.0. In brief, the solution mixture containing 10 μL of HRP (1 nM), 100 μL of ABTS (2 mM) and 20 μL of ZnO_2-ATM (Zn content: 2.0 mg mL^{-1} by ICP-MS) was incubated at RT for 0.5 h. The absorption of ABTS was measured to determine H_2O_2 generation. The H_2O_2 generation from Zn-ATM or ZnO_2 was measured using the same procedure.

To verify the ability of ATM as a CAT inhibitor, a solution mixture containing 5 mL of water, 20 μL of H_2O_2 (8 M), 50 μL of CAT (100 μg mL^{-1}) and 50 μL of ATM (10 mg mL^{-1}) was incubated at RT for 2 h, and the amount of O_2 produced was measured by using a dissolved oxygen meter. Similarly, a solution mixture containing 5 mL of water, 20 μL of H_2O_2 (8 M), 50 μL of CAT (100 μg mL^{-1}) and 500 μL of the corresponding nanoparticles (Zn content: 2.0 mg mL^{-1} by ICP-MS) was incubated, and the amount of O_2 produced was measured by using a dissolved oxygen meter.

Oxidative stress elevation *in vitro*

Mouse macrophage RAW264.7 cells and mouse breast 4T1 cancer cells were obtained from the National Collection of Authenticated Cell Cultures. The cells were incubated at 37.0 °C within 5% CO_2 and cultured in Dulbecco's modified Eagle's medium (DMEM) supplemented with 10% fetal bovine serum (FBS) and 1% penicillin/streptomycin. The entire process of cell culture followed American Type Culture Collection (ATCC) instructions.

To study the resistance activity of different cells to H_2O_2 and $^{\bullet}OH$, RAW264.7 macrophages (1×10^4 cells per dish) or 4T1 cells (5×10^3 cells per dish) were seeded into 1 mL culture dishes for 24 h. Afterwards, 1 mL of the cells were treated with 100 μL different concentrations of H_2O_2 and $^{\bullet}OH$ (from 0 to 20 mM), respectively. The $^{\bullet}OH$ was obtained by incubating equal concentrations of H_2O_2 with appropriate amounts of HRP. After another 6 h incubation, apoptosis/necrosis of these cells was measured by using an Annexin V-FITC/PI. Meanwhile. RAW264.7 macrophages were collected and stained by using CD206-PE and CD80-APC. Cellular fluorescence was analyzed by flow cytometry.

To investigate *in vitro* ROS-generating activity, confocal images were obtained within cancer cells by using DCFH-DA, and 4T1 cells were seeded into 0.3 mL culture dishes (5×10^3 cells per dish) for 24 h. Afterwards, cells were treated with Zn^{2+}, ATM, Zn-ATM, ZnO_2 and ZnO_2-ATM, respectively (5 μL, Zn content: 2.0 mg mL^{-1}; ATM content: 1.0 mg mL^{-1}). After another 6 h incubation, DCFH-DA (1 μM) and Hoechst (1 μg mL^{-1}) were added into each well and incubated for another 20 min at 37.0 °C. Fluorescence images were captured by CLSM.

JC-1 staining

To investigate the *in vitro* mitochondrial potential, confocal images were measured within cancer cells by using JC-1, and 4T1 cells were seeded into 0.3 mL culture dishes (5×10^3 cells per dish) for 24 h. Afterwards, the cells were treated with Zn^{2+}, ATM, Zn-ATM, ZnO_2 and ZnO_2-ATM, respectively (5 μL, Zn content: 2.0 mg mL^{-1}; ATM content: 1.0 mg mL^{-1}). After another 4 h incubation, cells were stained by using JC-1 (10 μg mL^{-1}) and Hoechst (1 μg mL^{-1}) for another 20 min at 37.0 °C. Fluorescence images were captured by CLSM.

In vitro antitumor effect

To measure the cellular viability, 4T1 cells were cultivated in a 96-well plate and incubated with different concentrations of Zn^{2+}, ATM, Zn-ATM, ZnO_2 and ZnO_2-ATM, respectively. After incubation for 6 h, cellular viability was tested by using MTT assay.

Immunogenic cell death

To investigate *in vitro* ATP release, 4T1 cells were cultivated in a 6-well culture plate (1×10^5 cells per dish) for 24 h. Afterwards, cells were treated with Zn^{2+}, ATM, Zn-ATM, ZnO_2 and ZnO_2-ATM, respectively (20 μL, Zn content: 2.0 mg mL^{-1}; ATM content: 1.0 mg mL^{-1}), for another 24 h incubation. After centrifugation at 4000 rpm for 10 min, cell supernatants were collected. The content of ATP in the supernatant was quantified using an ATP assay kit.

For CRT staining, 4T1 cells were cultivated in a 24-well culture plate (5×10^4 cells per dish) for 24 h. Afterwards, cells were treated with Zn^{2+}, ATM, Zn-ATM, ZnO_2 and ZnO_2-ATM, respectively (5 μL, Zn content: 2.0 mg mL^{-1}; ATM content: 1.0 mg mL^{-1}), for another 4 h incubation. Then cells were incubated with anti-CRT primary antibodies at RT for 0.5 h and stained with APC-conjugated secondary antibodies for 2 h. For HMGB-1 staining, cells were treated with anti-HMGB primary antibodies at RT for 0.5 h and incubated with Alexa Fluor 594-conjugated secondary antibodies for 2 h. The nuclei were stained by using DAPI at room temperature for 30 min. Fluorescence images were captured by CLSM.

In vitro macrophage polarization

RAW264.7 cells were plated in a 24-well plate (1×10^5 per well) and then cultured with LPS (500 ng mL^{-1}) or IL-4 (25 ng mL^{-1}) for 12 h to induce M1 or M2 polarization, respectively. 2.5 μL of Zn^{2+}, ATM, Zn-ATM, ZnO_2 and ZnO_2-ATM (Zn content: 2.0 mg mL^{-1}; ATM content: 1.0 mg mL^{-1}) were incubated with RAW264.7 cells for another 12 h. Afterwards, RAW264.7 cells were collected and stained by using CD206-PE and CD80-APC. Cellular fluorescence was analyzed by flow cytometry. Moreover, cell supernatants were collected to detect the content changes in IL-6 and TNF-α by using ELISA kits.

Antitumor effect *in vivo*

All animal protocols and all injection procedures and post-operative care were approved by the Ethical Committee of Qufu Normal University (No: 2022013). Balb/c mice were subjected to subcutaneous injection of 4T1 cells at both the right

(1×10^6 cells) and the left flanks (3×10^5 cells), which were termed primary and distant (metastatic) tumors, respectively.

Mice were divided into six groups randomly (9 mice for each group). After tumor sizes reached ~100 mm^3, various treatments, including (1) DPBS, (2) Zn^{2+}, (3) ATM, (4) Zn-ATM, (5) ZnO_2 and (6) ZnO_2-ATM, were intratumorally injected into the primary tumors at a dosage of 25 μL (Zn content: 2.0 mg mL^{-1}; ATM content: 1.0 mg mL^{-1}). From day 0, the tumor size and body weight of each mouse were monitored every 2 days. A caliper was used to measure the tumor volume and tumor size and then volume = length × $width^2/2$ was calculated. On day 1 post-injection, cryosections of primary tumors were collected from various groups for HE, TUNEL and CRT staining. Representative tumors were harvested on day 14 post-first injection, and organs were collected on day 14 post-first injection for H&E staining to assess pathologic changes.

On day 14 post-injection, distant tumors were collected from various groups for cryosections. A TUNEL apoptosis detection kit was used for TUNEL immunofluorescence staining through standard operating strategies. Finally, tumor slices were investigated by fluorescence confocal microscopy. Moreover, T cell infiltration within distant tumors was determined by staining with CD3-APC, CD4-PE and CD8a-FITC, followed by flow cytometry analysis. To demonstrate the antitumor immune memory effect of mice, the left flank of mice was rechallenged with 5×10^5 4T1 tumor cells through intravenous injection on day 18. All mice were sacrificed on day 44, and the lungs were stained by using 15% India ink for metastatic nodule counting.

In vivo macrophage polarization

On day 3 post-injection, the tumors of mice were collected, homogenized in PBS, and filtered through cell strainers to obtain a single cell suspension. Cells were dispersed in 2% BSA solution for 30 min to block nonspecific binding sites. Finally, the cell suspension of tumors was stained with CD11b-FITC, CD80-APC and CD206-PE for RAW264.7 phenotype analysis. Content changes of cytokines (IL-6 and TNF-α) in tumors were measured using ELISA kits.

Dendritic cell maturation and T cell infiltration within tumors

On day 3 post-injection, mice were sacrificed. Tumors and spleens were homogenized in PBS to obtain a single cell suspension and then washed with lysis buffer twice to remove erythrocytes. Cells were treated by using 2% BSA solution to block nonspecific binding sites for another 30 min. To investigate T cell infiltration within tumors, cell suspensions of tumors were stained by using CD3-APC, CD4-PE and CD8a-FITC and then analyzed by flow cytometry. To study the maturation of dendritic cells, cell suspensions of spleens were stained with CD11c-FITC, CD80-APC and CD86-PE. Then, cells were washed with PBS twice and analyzed with flow cytometry.

Immune memory effect against tumor recurrence

On day 20 post-injection, to validate the formation of memory T cells, mice were sacrificed for spleen collection. After homogenization and erythrocyte lysis, a single cell suspension of spleen was prepared. Cells were stained with CD3-APC, CD8a-FITC and CD44-PE following the manufacturers' protocol and analyzed with flow cytometry.

Statistical analysis

The significance of the statistical difference was determined through one-way analysis of variance (ANOVA) with $^*p < 0.05$, $^{**}p < 0.01$, $^{***}p < 0.001$, and $^{ns}p \geq 0.05$.

Conclusions

In this study, a bimodal responsive modulator, namely ZnO_2-ATM, has been developed, as an endo/exogenous synergistic H_2O_2-producing nano-based adjuvant, exerting a bimodal simultaneous implementation of TAM repolarization and ICD elicitation that contributed to tumor immunotherapy. The responsiveness of ZnO_2-ATM could elevate oxidative stress with varying effects on both tumor cells and immune cells, eventually eradicating both primary tumors and distant metastases. We anticipate that this selective and mechanistic strategy will completely overcome the obstacle of tumor immunosuppression in the future.

Data availability

All relevant data are presented in the article and the ESI.†

Author contributions

This manuscript was written through contributions from all authors. All authors have given approval to the final version of the manuscript. Y. Z. and W. K. contributed equally to this work. Y. Z. and W. K., conceptualization, formal analysis, investigation, data curation, funding acquisition and writing – original draft; J. Z., resources; F. Q., visualization, project administration, and funding acquisition.

Conflicts of interest

There are no conflicts to declare.

Acknowledgements

This work was financially supported by the National Key Research and Development Program of China (2021YFA0910100), the Pioneer Research and Development Program of Zhejiang (2022C03031 and 2023SDYXS0002), the National Natural Science Foundation of China (22274141, 22074080, 22207062, and 22304100), the Natural Science Foundation of Shandong Province (ZR2022ZD28, ZR2022QB223, and ZR2022QB209), and the Zhejiang Provincial Health Commission Research Foundation (WKJ-ZJ-242). Diagrams in Scheme 1, Fig. 1C and 3A were created with **https://www.biorender.com/**.

Notes and references

1 Y. Ren, R. Wang, S. Weng, H. Xu, Y. Zhang, S. Chen, S. Liu, Y. Ba, Z. Zhou, P. Luo, Q. Cheng, Q. Dang, Z. Liu and X. Han, *Mol. Cancer*, 2023, **22**, 130.
2 Z. Niu, Q. Shi, W. Zhang, Y. Shu, N. Yang, B. Chen, Q. Wang, X. Zhao, J. Chen, N. Cheng, X. Feng, Z. Hua, J. Ji and P. Shen, *Nat. Commun.*, 2017, **8**, 766.
3 C. Ngambenjawong, H. H. Gustafson and S. H. Pun, *Adv. Drug Delivery Rev.*, 2017, **114**, 206–221.
4 Y. Xue, X. Yan, D. Li, S. Dong and Y. Ping, *Nat. Commun.*, 2024, **15**, 2270.
5 H. S. Seo, J.-H. Han, J. Lim, G.-H. Bae, M. J. Byun, C.-P. J. Wang, J. Han, J. Park, H. H. Park, M. Shin, T.-E. Park, T.-H. Kim, S.-N. Kim, W. Park and C. G. Park, *Biomater. Res.*, 2024, **28**, 0008.
6 B. Wei, J. Pan, R. Yuan, B. Shao, Y. Wang, X. Guo and S. Zhou, *Nano Lett.*, 2021, **21**, 4231–4240.
7 H. Jiang, H. Fu, Y. Guo, P. Hu and J. Shi, *Biomaterials*, 2022, **289**, 121799.
8 J. Zhao, H. Huang, J. Zhao, X. Xiong, S. Zheng, X. Wei and S. Zhou, *Acta Pharm. Sin. B*, 2022, **12**, 2683–2694.
9 A. Buqué and L. Galluzzi, *Trends Cancer*, 2018, **4**, 599–601.
10 K. Parikh, C. Warren and R. Caracio, *J. Clin. Oncol.*, 2021, **39**, 478.
11 Y. Yin, X. Jiang, L. Sun, H. Li, C. Su, Y. Zhang, G. Xu, X. Li, C. Zhao, Y. Chen, H. Xu and K. Zhang, *Nano Today*, 2021, **36**, 101009.
12 C. Deng, Q. Zhang, M. Jia, J. Zhao, X. Sun, T. Gong and Z. Zhang, *Adv. Sci.*, 2019, **6**, 1801868.
13 Y. Sun, T. Lian, Q. Huang, Y. Chang, Y. Li, X. Guo, W. Kong, Y. Yang, K. Zhang, P. Wang and X. Wang, *J. Controlled Release*, 2023, **364**, 174–194.
14 D. V. Krysko, A. D. Garg, A. Kaczmarek, O. Krysko, P. Agostinis and P. Vandenabeele, *Nat. Rev. Cancer*, 2012, **12**, 860–875.
15 S. Bittner, K. Pape, L. Klotz and F. Zipp, *Nat. Rev. Neurol.*, 2023, **19**, 477–488.
16 A. M. Cameron, A. Castoldi, D. E. Sanin, L. J. Flachsmann, C. S. Field, D. J. Puleston, R. L. Kyle, A. E. Patterson, F. Hässler, J. M. Buescher, B. Kelly, E. L. Pearce and E. J. Pearce, *Nat. Immunol.*, 2019, **20**, 420–432.
17 Z. Feng, J. Guo, X. Liu, H. Song, C. Zhang, P. Huang, A. Dong, D. Kong and W. Wang, *Biomaterials*, 2020, **255**, 120210.
18 E. B. Higgs, R. Godschalk, S. A. S. Langie, F. J. van Schooten and N. J. Hodges, *Mutagenesis*, 2021, **36**, 437–444.
19 J.-H. Cheng, X. Lv, Y. Pan and D.-W. Sun, *Trends Food Sci. Technol.*, 2020, **103**, 239–247.
20 H. Jiang, X.-W. Zhang, Q.-L. Liao, W.-T. Wu, Y.-L. Liu and W.-H. Huang, *Small*, 2019, **15**, 1901787.
21 K. Liang, H. Sun, Z. Yang, H. Yu, J. Shen, X. Wang and H. Chen, *Adv. Funct. Mater.*, 2021, **31**, 2100355.
22 Z. Liao, D. Chua and N. S. Tan, *Mol. Cancer*, 2019, **18**, 65.
23 I. S. Harris and G. M. DeNicola, *Trends Cell Biol.*, 2020, **30**, 440–451.
24 S. Arfin, N. K. Jha, S. K. Jha, K. K. Kesari, J. Ruokolainen, S. Roychoudhury, B. Rathi and D. Kumar, *Antioxidants*, 2021, **10**, 642.
25 L. Wang, C. Lynch, S. P. Pitroda, A. Piffkó, K. Yang, A. K. Huser, H. L. Liang and R. R. Weichselbaum, *J. Exp. Med.*, 2024, **221**, e20232101.
26 Q. Liu, Y. Yang, M. Pan, F. Yang, Y. Yu and Z. Qian, *Theranostics*, 2024, **14**, 2304–2328.
27 P. Cui, Z. Chen, D. Gao, B. Zhao, W. Shi and P. Cheng, *Cryst. Growth Des.*, 2010, **10**, 4370–4378.
28 S. Verma and S. L. Jain, *Inorg. Chem. Front.*, 2014, **1**, 534–539.
29 S. Ahmad, M. Kharkwal, Govind and R. Nagarajan, *J. Phys. Chem. C*, 2011, **115**, 10131–10139.
30 P. Mahbub, C. K. Hasan, D. Rudd, N. H. Voelcker, J. Orbell, I. Cole and M. Macka, *Anal. Chim. Acta*, 2023, **1255**, 341156.
31 Z. Chen, D. Fu, K. Yuen Koh and J. Paul Chen, *Chem. Eng. J.*, 2022, **446**, 136845.
32 F. Cheng, L. He, J. Wang, L. Lai, L. Ma, K. Qu, Z. Yang, X. Wang, R. Zhao, L. Weng and L. Wang, *Nanoscale*, 2024, **16**, 18570–18583.
33 J. T. O. Cabrera and A. Makino, *Pharmacol. Ther.*, 2022, **229**, 107919.
34 C. Maueröder, R. A. Chaurio, T. Dumych, M. Podolska, M. D. Lootsik, S. Culemann, R. P. Friedrich, R. Bilyy, C. Alexiou, G. Schett, C. Berens, M. Herrmann and L. E. Munoz, *Cell Death Differ.*, 2016, **23**, 1016–1025.
35 F. Di Virgilio, V. Vultaggio-Poma, S. Falzoni and A. L. Giuliani, *Neuropharmacology*, 2023, **224**, 109333.
36 V. Vultaggio-Poma, A. C. Sarti and F. Di Virgilio, *Cells*, 2020, **9**, 2496.
37 A. Kusnadi, S. H. Park, R. Yuan, T. Pannellini, E. Giannopoulou, D. Oliver, T. Lu, K.-H. Park-Min and L. B. Ivashkiv, *Immunity*, 2019, **51**, 241–257.
38 L. Chen and J. Tang, *J. Clin. Oncol.*, 2020, **38**, e15570.
39 B. M. Hartmann, R. A. Albrecht, E. Zaslavsky, G. Nudelman, H. Pincas, N. Marjanovic, M. Schotsaert, C. Martínez-Romero, R. Fenutria, J. P. Ingram, I. Ramos, A. Fernandez-Sesma, S. Balachandran, A. García-Sastre and S. C. Sealfon, *Nat. Commun.*, 2017, **8**, 1931.
40 L. Yu, R. Feng, L. Zhu, Q. Hao, J. Chu, Y. Gu, Y. Luo, Z. Zhang, G. Chen and H. Chen, *Sci. Adv.*, 2020, **6**, eabb6595.
41 S. Starling, *Nat. Rev. Immunol.*, 2017, **17**, 730.
42 N. M. Chapman, M. R. Boothby and H. Chi, *Nat. Rev. Immunol.*, 2020, **20**, 55–70.